Eur. Phys. J. B **35**, 449–463 (2003)
DOI: 10.1140/epjb/e2003-00298-8

THE EUROPEAN PHYSICAL JOURNAL B

Hyperfine interaction of the 5d impurities in hexagonal Co

G. Seewald[1], B. Hinfurtner[1], E. Zech[1], E. Hagn[1], A. Burchard[2], D. Forkel-Wirth[2], R. Eder[2], and ISOLDE Collaboration[3]

[1] Physik-Department, Technische Universität München, 85748 Garching, Germany
[2] PPE Division, CERN, 1211 Geneva 23, Switzerland
[3] CERN, 1211 Geneva 23, Switzerland

Received 10 January 2003 / Received in final form 24 July 2003
Published online 24 October 2003 –

Abstract. The magnetic and electric hyperfine interaction frequencies of ^{197m}Hg, ^{191}Pt, ^{183}Os, and ^{183}Re in Co(hcp) were determined for parallel and perpendicular orientations of the magnetization relative to the c axis. Single-crystal samples were used, and the techniques of nuclear magnetic resonance on oriented nuclei and modulated adiabatic fast passage on oriented nuclei were applied. In addition, the nuclear spin-lattice relaxation constants in Co(hcp) were determined for ^{188}Ir, ^{183}Os, and ^{183}Re. The descriptions of the magnetization behaviour and the anisotropy of the hyperfine interaction were tested in detail for ^{191}Pt. The available data on the hyperfine interaction of the $5d$ elements in Co(hcp) are compiled. The use of these data to obtain information on the electronic structure of these systems, and in particular on the orbital part of the magnetism, is discussed.

PACS. 76.60.Jx Effects of internal magnetic fields – 75.50.Cc Ferromagnetic metals and alloys – 76.80.+y Mössbauer effect; other γ-ray spectroscopy

1 Introduction

The hyperfine fields at impurities in Fe, Co, and Ni have been used for some time as a testing ground for the description of the transition-metal magnetism by band structure calculations [1–4]. On the one hand, the range of potential impurities from Li to the actinides allows a wide variation of some important parameters of the investigated system. On the other hand, the impurity problem is a simple example for an artificially composed transition-metal compound. In this sense, it mediates directly to more elaborate systems like multilayers, but is usually easier to realize experimentally than, for example, well-defined interfaces.

Co and in particular its hexagonal phase — the hexagonal (hcp) phase is the stable phase below about 420 °C, but the cubic (fcc) phase can coexist as metastable phase — have so far received less attention as host matrix than Fe and Ni, where the impurity hyperfine fields have been studied experimentally and theoretically for most elements. This has mainly technical reasons: Single-crystal samples are required to ensure a pure hcp phase and to determine the anisotropy of the hyperfine interaction. The impurities must be implanted and the hyperfine interaction must be studied by radiation-based methods. However, apart from the larger experimental effort, the host Co(hcp) also offers some new insights.

Due to the hexagonal symmetry, the hyperfine field depends on the angle between the magnetization and the c axis. This anisotropy arises from the anisotropy of the orbital moment and from the noncubic spin distribution [5,6]. The anisotropy of the orbital moment is of particular interest, since it is directly related to the magnetic anisotropy energy and the magnetostriction [7,8], and since recently several schemes were developed for the self-consistent treatment of such phenomena within first principles calculations [9,10].

The spin-orbit-coupling-induced electric field gradient (spin-orbit EFG) provides a complementary approach to the study of the orbital part of the magnetism, as shown in a recent study of that effect in cubic Fe, Co, and Ni [11,12]. The effect probes the modification of the electronic density by the spin-orbit coupling and should also be present in hexagonal ferromagnetic hosts. The experimental separation from the lattice-symmetry-induced electric field gradient (lattice EFG) requires the measurement of the EFG for different angles between the magnetization and the c axis.

Moreover, the hyperfine fields in Co(hcp) and Co(fcc) typically differ much more than the densities and magnetizations of the two Co phases, which are identical within 2%. This allows one to study specifically the influence of the lattice symmetry on the hyperfine interaction.

Studies of the magnetic and electric parts of the hyperfine interaction in Co(hcp) that also investigate the dependence on the angle between the magnetization and the c axis are still available only for a few impurities: Such studies have been performed for Co [6,13,14], Fe [5], Br [15], Lu [16], Ir [17,18], Pt [19], and Au [20]. In this work we present data on Hg, Os, and Re and improved data on Pt. In addition, the nuclear spin-lattice relaxation constants are given for Re to Au. For the $5d$ impurities now a fairly complete study of the systematics of the hyperfine interaction in Co(hcp) is possible.

2 Hyperfine interaction in Co(hcp)

2.1 Magnetization behaviour

The external magnetic field $\mathbf{B}_{\rm ext}$ was applied either parallel to the c axis (0° geometry) or perpendicular to the c axis (90° geometry). In the 0° geometry the magnetization remains parallel to the c axis, the easy direction of magnetization. In the 90° geometry the magnetization is rotated towards $\mathbf{B}_{\rm ext}$. The orientation perpendicular to the c axis is obtained at $B_{\rm ext} \geq B_a$, where $B_a = 1.35$ T is the anisotropy field.

Due to unavoidable misalignments, the "orientation angle" α between the magnetic field and the c axis was in general not exactly 0° or 90°. In the 0° geometry the misalignment could be neglected. However, in the 90° geometry the magnetization behaviour is extremely sensitive to α, especially around $B_{\rm ext} = B_a$. Therefore, in that geometry the actual value of α had to be taken into account.

The angle θ between the magnetization and the c axis was calculated as a function of $B_{\rm ext}$ and α by finding the minimum of the free energy $F(\theta, \alpha, B_{\rm ext})$ as a function of θ. F is given by

$$F = K_1 \sin^2\theta + K_2 \sin^4\theta - B_{\rm ext} M \cos(\alpha - \theta) \\ -(1/2)\mathbf{M}\mathbf{B}_{\rm dem}. \quad (1)$$

The anisotropy constants $K_1 = 0.766$ J/cm^{-3} and $K_2 = 0.105$ J/cm^{-3} and the magnetization $M = 0.1442$ T were taken from reference [21]. The same value of M was used as in reference [21], because in that work rather K_i/M than K_i was determined.

The last term of equation (1) is the demagnetization energy. The demagnetization field $\mathbf{B}_{\rm dem}$, which was of the order of 0.05 T, is a function of the sample shape and the distribution of the magnetization in the sample. An exact treatment of the demagnetization energy would be rather involved. Therefore, it was treated within the two-domain model that is described in Appendix A.

2.2 Magnetic hyperfine splitting

The magnetic resonance frequency is given by

$$\nu_m = \frac{g\mu_N}{h} \left|\mathbf{B}_{\rm HF} + (1+K)(1-\sigma)(\mathbf{B}_{\rm ext} + \mathbf{B}_{\rm dem})\right|. \quad (2)$$

Here g is the nuclear g factor, μ_N is the nuclear magneton, K is the Knight shift, σ is the diamagnetic shielding, and $\mathbf{B}_{\rm HF}$ is the hyperfine field, which depends in general on the orientation of the magnetization. The components parallel and perpendicular to the c axis, $B^z_{\rm HF}$ and $B^x_{\rm HF}$, are given by

$$B^z_{\rm HF} = (B^{\rm iso}_{\rm HF} + B^{\rm ani}_{\rm HF})\cos\theta, \\ B^x_{\rm HF} = (B^{\rm iso}_{\rm HF} - \tfrac{1}{2}B^{\rm ani}_{\rm HF})\sin\theta, \quad (3)$$

where $B^{\rm iso}_{\rm HF}$ and $B^{\rm ani}_{\rm HF}$ are the isotropic and anisotropic parts of the hyperfine field, respectively. The shielding of $\mathbf{B}_{\rm ext}$ by $\mathbf{B}_{\rm dem}$ was described within the two-domain model. The respective expressions for $\mathbf{B}_{\rm ext} + \mathbf{B}_{\rm dem}$ are given in Appendix A.

2.3 Electric hyperfine splitting

The EFG causes a quadrupole splitting of the resonance spectrum into $2I$ approximately equidistant subresonances with subresonance separation $\Delta\nu_Q$. The subresonance between the states with magnetic quantum numbers m and $m+1$ is given by

$$\nu_{m\to m+1} = \nu_m - \Delta\nu_Q(m + \tfrac{1}{2}). \quad (4)$$

The subresonance between the most populated sublevels $m = I$ and $m = (I-1)$ is referred to as the ν_1 resonance, the subresonance between $m = (I-1)$ and $m = (I-2)$ as the ν_2 resonance, and so on.

The EFG is the sum of two contributions: The lattice EFG, with principal component $V^{\rm lat}_{zz}$, is axially symmetric relative to the c axis and arises from the noncubic lattice symmetry. The usually considerably smaller spin-orbit EFG, with principal component $V^{\rm so}_{z'z'}$, is axially symmetric relative to the direction of the magnetization and arises, via the spin-orbit coupling, from the magnetism. Both contributions can be separated via the anisotropy of $\Delta\nu_Q$:

$$\Delta\nu_Q = \frac{3}{2I(2I-1)} \frac{eQ}{h} \left(V^{\rm lat}_{zz} P_2(\cos\theta) + V^{\rm so}_{z'z'}\right). \quad (5)$$

Here P_2 is the Legendre polynomial of second order and eQ is the nuclear quadrupole moment.

The subresonances are exactly equidistant only for $\theta = 0°$ or in the limit $\Delta\nu_Q/\nu_m \to 0$. For $\theta \neq 0°$, the exact subresonance positions were obtained by numerical diagonalization of the full Hamiltonian of the combined hyperfine interaction. The quantity $\Delta\nu_Q$ is then defined by equation (5).

As shown in Appendix B, $V^{\rm so}_{z'z'}$ depends in the following way on the direction of the magnetization:

$$V^{\rm so}_{z'z'}(\theta) = V^{{\rm so}(0)}_{z'z'} + V^{{\rm so}(2)}_{z'z'} P_2(\cos\theta) + V^{{\rm so}(4)}_{z'z'} P_4(\cos\theta). \quad (6)$$

Therefore, in principle equation (5) has to be replaced by an expansion of $\Delta\nu_Q$ into a P_0, a P_2, and a P_4 term, which can be attributed to $V^{{\rm so}(0)}_{z'z'}$, $V^{\rm lat}_{zz} + V^{{\rm so}(2)}_{z'z'}$, and $V^{{\rm so}(4)}_{z'z'}$, respectively.

However, the data could perfectly be described without anisotropy of the spin-orbit EFG. Moreover, the model calculations of Appendix B suggest that $V_{z'z'}^{\mathrm{so}(4)}/V_{z'z'}^{\mathrm{so}(0)}$ and $V_{z'z'}^{\mathrm{so}(2)}/V_{z'z'}^{\mathrm{so}(0)}$ are only of the order of 10%. Therefore, the anisotropy of the spin-orbit EFG was neglected in favour of a more compact data presentation. This approximation is unlikely to introduce major errors in the separation of the lattice and spin-orbit parts of the EFG. However, one should be aware that the quoted V_{zz}^{lat} may contain a contribution from $V_{z'z'}^{\mathrm{so}(2)}$, and that a significant $V_{z'z'}^{\mathrm{so}(4)}$ can be excluded only in those cases where the quadrupole splitting was determined for more than two substantially different θ's.

2.4 Interpretation of the measurements

The following five parameters were used to characterize the hyperfine splitting of a given isotope:

$$\nu_m^{\parallel} = |g\mu_N B_{\mathrm{HF}}(\theta = 0°)/h|, \tag{7}$$

$$\nu_m^{\perp} = |g\mu_N B_{\mathrm{HF}}(\theta = 90°)/h|, \tag{8}$$

$$d\nu/dB_{\mathrm{ext}} = |g\mu_N/h|\mathrm{sgn}(B_{\mathrm{HF}})(1+K)(1-\sigma), \tag{9}$$

$$\Delta\nu_Q^{\parallel} = \Delta\nu_Q(\theta = 0°), \tag{10}$$

$$\Delta\nu_Q^{\perp} = \Delta\nu_Q(\theta = 90°). \tag{11}$$

To obtain this parameter set, resonance spectra were measured in the 0° and 90° geometries for different magnetic fields. Each spectrum was interpreted in terms of ν_1 and $\Delta\nu_Q$. The hyperfine interaction parameters together with α in the 90° geometry and the demagnetization fields, $B_{\mathrm{dem}}^{(0),\parallel}$ and $B_{\mathrm{dem}}^{(0),\perp}$, were then obtained via *least squares* fit to this data set.

The problem that θ and $\Delta\nu_Q^{\perp}/\Delta\nu_Q^{\parallel}$ must in general already be known to deduce the exact value of $\Delta\nu_Q$ (as defined by Eq. (5)) from the resonance spectrum, was solved by an iterative procedure.

An error of the anisotropy constants of 1% was taken into account. Moreover, some parameters had to be estimated, if not enough data were available to determine all parameters. $d\nu/dB_{\mathrm{ext}}$ was estimated assuming $K = 0.00(1)$ and taking σ from reference [22]. $|\alpha - 90°| < 1°$ in the 90° geometry and $B_{\mathrm{dem}}^{(0),\perp} = 0.05 \pm 0.03$ T could be inferred from several experiments where these parameters had been determined for the same setup and similar sample shapes.

2.5 Nuclear spin-lattice relaxation

The nuclear spin-lattice relaxation rates are quoted in form of the inverse Korringa constant $R = (T_1T)^{-1}$ or in form of the "reduced" relaxation constant R/g^2, which is independent of the spin and the magnetic moment of the investigated isotope. In hexagonal metals R depends in general on the angle between the quantization axis and the c axis. Accordingly, $R^{\parallel}$ and $R^{\perp}$, the relaxation constants for parallel and perpendicular orientations of the magnetization relative to the c axis, can be distinguished.

In ferromagnetic Fe, Co, and Ni, the magnetic field dependence of the relaxation complicates the situation [23–25]. Only the high-field limits are commonly compared with the predictions of the ab initio calculations [26]. Detailed studies of the field dependence of the spin-lattice relaxations of ^{198}Au [27] and ^{111}In [28] in Co(hcp) showed that the relaxation at zero field already represents the high-field limit. This can be understood as a consequence of the rather large anisotropy field of Co(hcp).

3 Experimental details and techniques

The radioactive impurities were produced at the on-line mass separator ISOLDE at CERN by spallation reactions of 1 GeV protons on a liquid Pb target. Hg isotopes of the desired mass were implanted into the Co(hcp) samples using a voltage of 60 kV. Via the decay of the Hg precursors suitable radioactive 5d impurities are available from Re to Hg. The activity was implanted within an area of the order of 0.15 cm^2. The resulting impurity concentrations were always less than 10^{-4}.

The used Co(hcp) single-crystal disks were about 0.3 mm thick and 1.2 cm in diameter, with the c axis in the plane and one straight edge perpendicular to the c axis to facilitate the orientation on the sample holder. The linewidths of the resonance spectra turned out to depend crucially on the surface preparation of the Co samples. The electropolishing of the samples in 85% H_3PO_4 (about 30 min, $U = 1.4$ V, graphite cathode, Pt sample holder) after careful mechanical polishing has proved to give good results.

After the implantation the samples were mounted into a ^{3}He-^{4}He dilution refrigerator and cooled down to temperatures in the 10 mK range. The temperature was monitored by a separate ^{60}CoCo(hcp) nuclear orientation thermometer. Particular attention was paid to the orientation of the c axis with respect to $\mathbf{B}_{\mathrm{ext}}$, which was accurate within 1°.

The resonance spectra were measured by nuclear magnetic resonance on oriented nuclei (NMR-ON) [29]. In this NMR technique the resonance is detected via changes in the anisotropic emission of the γ radiation of oriented radioactive probe nuclei. The γ anisotropy was measured by four Ge detectors, which were placed at 0°, 90°, 180°, and 270° with respect to the magnetic field. The following ratio of the individual count rates was used throughout to analyse the data:

$$\epsilon = \frac{W(0°) + W(180°)}{W(90°) + W(270°)} - 1.$$

If the subresonance structure is hidden by the inhomogeneous broadening of the resonance, $\Delta\nu_Q$ can be determined by modulated adiabatic fast passage on oriented nuclei (MAPON): Two rf fields with fixed frequency separation $\Delta\nu$ are swept over the resonance in a time that

is short with respect to the relaxation time. The response of the γ anisotropy is recorded as a function of $\Delta\nu$. This so called MAPON spectrum is, apart from an offset, proportional to the integral $\int_0^{\Delta\nu} P(\Delta\nu_Q)\, d\Delta\nu_Q$ of the distribution $P(\Delta\nu_Q)$ of the subresonance separation. For more details on the MAPON technique we refer to references [30–32]. The sign of $\Delta\nu_Q$ can be deduced from the characteristic form of the relaxation curve after the MAPON sweep [31,33].

The nuclear spin-lattice relaxation was measured by NMR-ON: The frequency modulation (FM) was switched on and, after some time, switched off again. Due to the inhomogeneous broadening of the resonance, virtually no nuclei are excited without FM. R was obtained via *least squares* fit to the resulting relaxation curve [25,34].

4 Experimental results

4.1 HgCo(hcp)

About 5×10^{11} ^{197m}Hg nuclei ($I^\pi = 13/2^+$, $T_{1/2} = 23.8$ h) and a comparable amount of ^{197}Hg nuclei were implanted. The hyperfine interaction of ^{197m}Hg was investigated via the 133 keV transition in the decay to the ground state.

NMR-ON and MAPON spectra were measured in the 0° geometry at zero field and in the 90° geometry at $B_{\rm ext}$ = 2 T. Figure 1 shows the NMR-ON spectra. The large linewidths of over 1%, which are for $M \parallel c$ about twice as large as for $M \perp c$, are mainly due to the unresolved quadrupole splitting. $\bar{\nu} - \nu_m$, the displacement of the resonance by the quadrupole splitting, was estimated by model calculations as $-3.5(10) \times \Delta\nu_Q$. If that displacement and the shift of the resonance in the external field are taken into account, one obtains

$$\nu_m^{\parallel} = 78.91(50)\ \text{MHz},$$

$$\nu_m^{\perp} = 76.29(24)\ \text{MHz}.$$

The error comes mainly from the estimation of $\bar{\nu} - \nu_m$.

Figure 2 shows the MAPON spectra. The following quadrupole splittings were deduced:

$$\Delta\nu_Q^{\parallel} = -0.496(4)\ \text{MHz},$$

$$\Delta\nu_Q^{\perp} = +0.239(5)\ \text{MHz}.$$

The signs were deduced from the form of the relaxation curves after the MAPON sweep. The characteristic difference in the form between sweep up and sweep down is shown for the 0° geometry in Figure 3. The quoted $\Delta\nu_Q^{\perp}$ takes into account that the actual subresonance separations in the 90° geometry are all different and deviate from $\Delta\nu_Q$ by up to ±0.007 MHz. The resulting displacement of the MAPON spectrum by the different weighting of the different subresonance separations was estimated as +0.005(1) MHz.

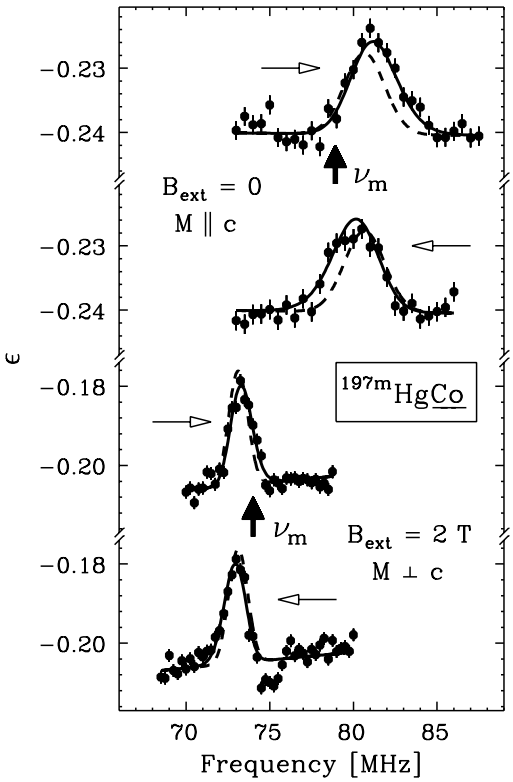

Fig. 1. ^{197m}HgCo(hcp): NMR-ON spectra in the 0° and 90° geometries. Because the relaxation back to thermal equilibrium was not awaited before applying (every 150 s) the next frequency, the resonances are displaced along the propagation directions of the rf frequency (indicated by the open arrows). The dashed curves are the resonance spectra without relaxation effects. The solid arrows mark the positions of ν_m. $T \approx$ 28 mK in the 0° geometry and ≈ 25 mK in the 90° geometry.

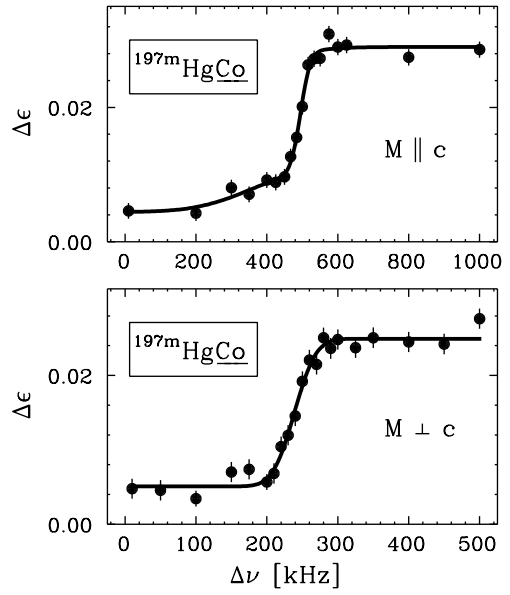

Fig. 2. ^{197m}HgCo(hcp): MAPON spectra. Top: 0° geometry, $B_{\rm ext}$ = 0 T. Bottom: 90° geometry, $B_{\rm ext}$ = 2 T. The carrier frequency was swept in 4 s from 78.5 MHz to 82.5 MHz in the 0° geometry and from 76.5 MHz to 71.5 MHz in the 90° geometry.

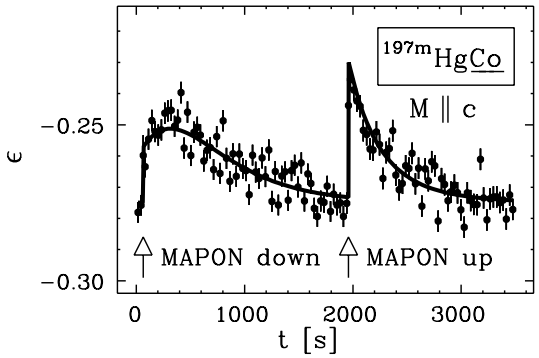

Fig. 3. ^{197m}HgCo(hcp): MAPON relaxation curves for different sweep directions. 0° geometry, $B_{\rm ext} = 0$ T, $\Delta\nu = 1$ MHz, sweep between 73.5 MHz and 82.5 MHz in 8 s. Although the relaxation curves were somewhat modified by the periodic heating of the sample during the sweep, the characteristic difference between sweep up and sweep down is clearly visible.

The MAPON technique also gives information on the inhomogeneous broadening of $P(\Delta\nu_Q)$. The half-widths were $\Gamma_Q = 0.077(12)$ MHz in the 0° geometry and $\Gamma_Q = 0.063(10)$ MHz in the 90° geometry. Moreover, in the 0° geometry a second, considerably smaller and much broader component of $P(\Delta\nu_Q)$ can be distinguished, which is attributed to probe nuclei with slightly disturbed surroundings.

4.2 PtCo(hcp)

To study the hyperfine interaction of ^{191}Pt($I^\pi = 3/2^+$, $T_{1/2} = 2.8$ d), about 2×10^{12} $A = 191$ nuclei were implanted. The field dependence of the hyperfine interaction was investigated in detail: NMR-ON measurements were performed in the 0° geometry between 0.01 and 0.6 T and in the 90° geometry between 0.95 and 2.0 T. Figure 4 shows NMR-ON spectra for the two limiting cases $\theta = 0°$ and $\theta \approx 90°$. Figure 5 shows the evolution of the subresonance structure in the 90° geometry from $\theta \approx 49°$ at $B_{\rm ext} = 0.95$ T to $\theta \approx 55°$ at $B_{\rm ext} = 1.05$ T, where the quadrupole splitting changes the sign and the three subresonances coincide, to $\theta \approx 90°$ for $B_{\rm ext} > B_a$.

The *least squares* fit analysis of the data yielded the following set of parameters:

$$\nu_m^{\parallel} = 235.21(2)\ \text{MHz},$$
$$\nu_m^{\perp} = 232.14(3)\ \text{MHz},$$
$$\Delta\nu_Q^{\parallel} = +13.54(2)\ \text{MHz},$$
$$\Delta\nu_Q^{\perp} = -6.83(2)\ \text{MHz},$$
$$d\nu/dB_{\rm ext} = -2.45(4)\ \text{MHz/T},$$
$$\alpha(90°) = 89.66(5)°,$$
$$B_{\rm dem}^{(0),\parallel} = 0.027(4)\ \text{T},$$
$$B_{\rm dem}^{(0),\perp} = 0.035(3)\ \text{T}.$$

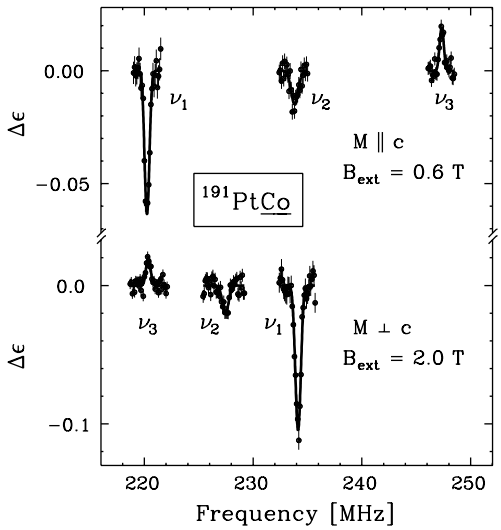

Fig. 4. ^{191}PtCo(hcp): NMR-ON spectra in the 0° geometry at $B_{\rm ext} = 0.6$ T (top) and in the 90° geometry at $B_{\rm ext} = 2.0$ T (bottom).

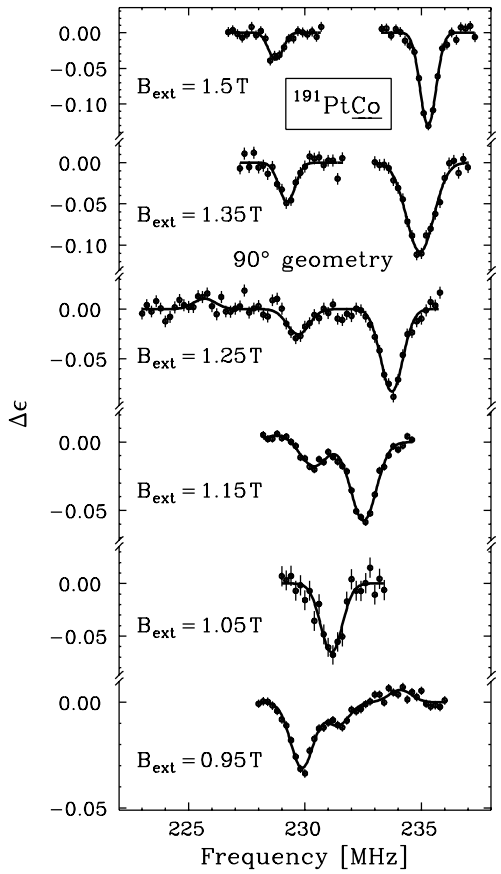

Fig. 5. ^{191}PtCo(hcp): NMR-ON spectra in the 90° geometry.

The respective theoretical description is compared with the experimental hyperfine splitting frequencies in Figures 6 and 7. The perfect agreement confirms the validity of the used descriptions of the magnetization behaviour and the anisotropy of the hyperfine interaction. $d\nu/dB_{\rm ext}$ agrees with $-2.47(4)$ MHz/T, the shift of the resonance that is expected for $g(^{191}\text{Pt}) = 0.329(5)$ [35] and $K = 0$.

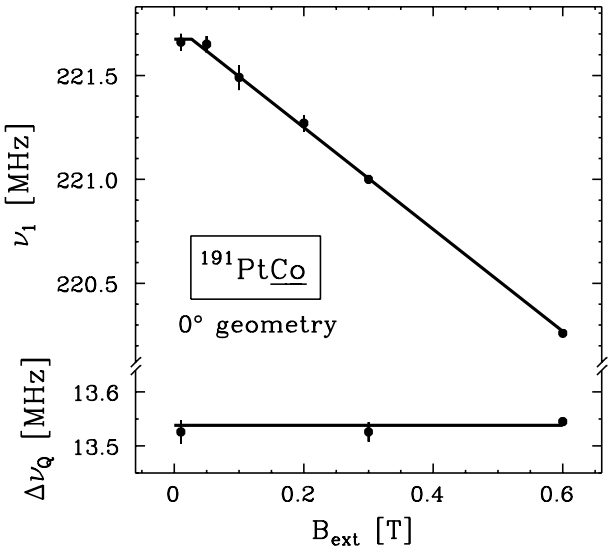

Fig. 6. ^{191}PtCo(hcp): Magnetic field dependence of ν_1 and $\Delta\nu_Q$ in the 0° geometry.

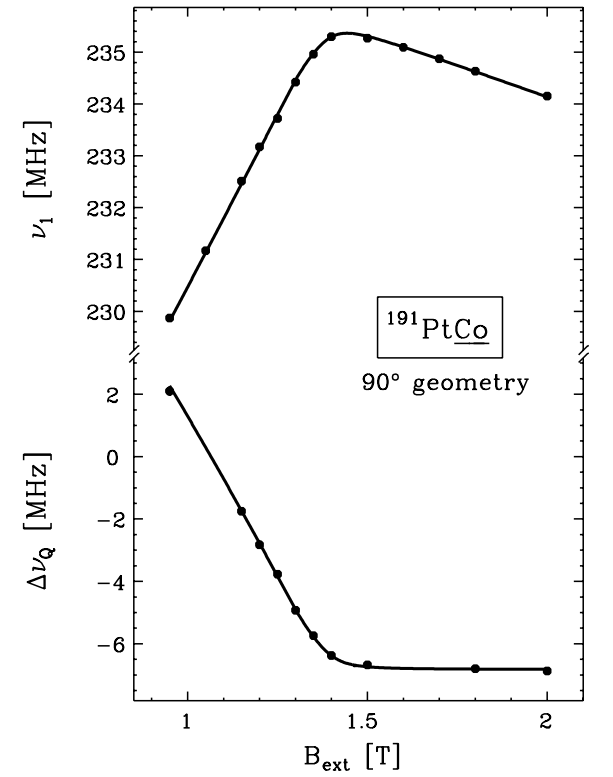

Fig. 7. ^{191}PtCo(hcp): Magnetic field dependence of ν_1 and $\Delta\nu_Q$ in the 90° geometry.

The hyperfine interaction of ^{191}PtCo(hcp) had already been studied in a previous work [19]. However, in that experiment a relatively thick sample was used, less attention was paid to the orientation of the c axis, and the surface preparation was less perfect. Consequently, the line widths of the resonances were much larger, $\Delta\nu_Q^{\parallel}$ deviated by about 1% from the present result, and in the 90° geometry the quadrupole splitting deviated even at 2.0 T still by about 10% from the correct $\Delta\nu_Q^{\perp}$. This demonstrates the importance of the refined surface preparation and of the control of small deviations from $\alpha = 90°$ for the precise determination of the hyperfine interaction.

4.3 IrCo(hcp)

The hyperfine interactions of several Ir isotopes in Co(hcp) were studied in references [17,18]. Since the emphasis in that work was on the EFG and the quadrupole moments, the magnetic hyperfine splitting frequencies were not given. This is done now in Table 1 for those isotopes where both $\nu_m^{\parallel}$ and $\nu_m^{\perp}$ were determined. The reproducibility of the results is demonstrated by the good agreement of all $\nu_m^{\perp}/\nu_m^{\parallel}$'s.

The magnetic hyperfine splitting frequencies also provide information on the hyperfine anomaly (HFA). The HFA $^1\Delta^2$ between the isotopes "1" and "2" is defined by

$$(\nu_m^{(1)}/\nu_m^{(2)}) = (g^{(1)}/g^{(2)})(1 + {}^1\Delta^2), \qquad (12)$$

where $\nu_m^{(1)}$, $\nu_m^{(2)}$, $g^{(1)}$, and $g^{(2)}$ are the magnetic hyperfine splitting frequencies and g factors of the respective isotopes. A large HFA is expected between ^{189}Ir on the one hand and ^{184}Ir, ^{186}Ir, and ^{188}Ir on the other hand. According to the Moskowitz-Lombardi rule [38], it can be estimated to be $^{189}\Delta_c^{184,186,188} = +0.089(15)$ for a pure contact field.

The HFA in Co(hcp), $^{189}\Delta^{186}_{\mathrm{Co(hcp)}}$, cannot be determined directly, since no independent information on the g factors of the respective Ir isotopes is available. However, the HFA's in Co(hcp) and Fe can be compared with high precision. From the data of Table 1 we deduce

$$^{189}\Delta^{186}_{\mathrm{Co(hcp)}} - {}^{189}\Delta^{186}_{\mathrm{Fe}} = -0.0011(8).$$

Consistent, but less precise information on the HFA has already been obtained by Mössbauer effect studies on ^{193}Ir in Co(hcp) [39].

4.4 OsCo(hcp)

The experiment on ^{183}Os ($I^{\pi} = 9/2^+$, $T_{1/2} = 13$ h) was limited by the comparatively short half-life and the small activity of the sample: Since the Hg yields at ISOLDE decline rapidly with decreasing mass number for $A < 185$, only about $4{\times}10^{10}$ $A = 183$ nuclei could be collected during 8 h of implantation. Therefore, only two measurements of the complete subresonance structure could be performed, at $B_{\mathrm{ext}} = 1.5$ T in the 90° geometry and at $B_{\mathrm{ext}} = 0$ T in the 0° geometry. In addition, in the 90° geometry the ν_1 resonance was measured at $B_{\mathrm{ext}} = 1.4$ T and 1.7 T. The resonance spectra are shown in Figure 8.

The presence of a large spin-orbit EFG reveals itself in a large deviation of $\Delta\nu_Q^{\perp}/\Delta\nu_Q^{\parallel}$ from $-1/2$: The quadrupole splitting in the 90° geometry is rather a factor of 2 larger

Table 1. Magnetic hyperfine splitting frequencies of several Ir isotopes in Co(hcp) and in Fe for $M\|[100]$ ($\nu_{m,\mathrm{Fe}}^{[100]}$ from references [36] and [37]).

Isotope	$\nu_m^{\parallel}$ (MHz)	$\nu_m^{\perp}$ (MHz)	$\nu_m^{\perp}/\nu_m^{\parallel}$	$\nu_{m,\mathrm{Fe}}^{[100]}$ (MHz)	$\nu_m^{\parallel}/\nu_{m,\mathrm{Fe}}^{[100]}$
^{184}Ir	108.13(13)	108.22(9)	1.0008(15)		
^{186}Ir	598.07(8)	598.20(17)	1.0002(3)	794.68(20)	0.7526(2)
^{188}Ir	238.07(1)	238.11(5)	1.0002(2)	316.25(14)	0.7528(3)
^{189}Ir	77.07(5)	77.11(17)	1.0005(23)	102.512(17)	0.7518(5)

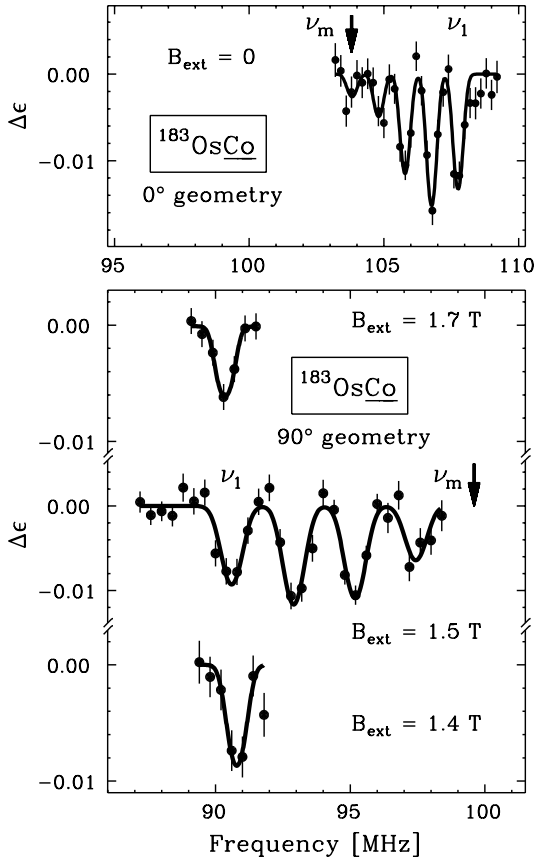

Fig. 8. ^{183}OsCo(hcp): NMR-ON spectra in the 0° and 90° geometries.

instead of being a factor of 2 smaller than the quadrupole splitting in the 0° geometry. The *least squares* fit yielded $\alpha > 89.5°$ and

$$\nu_m^{\parallel} = 103.82(6)\mathrm{MHz},$$
$$\nu_m^{\perp} = 101.53(12)\mathrm{MHz},$$
$$\Delta\nu_Q^{\parallel} = -0.984(18)\mathrm{MHz},$$
$$\Delta\nu_Q^{\perp} = +2.246(42)\mathrm{MHz}.$$

4.5 ReCo(hcp)

The sample of the ^{183}OsCo(hcp) experiment was used after the decay of ^{183}Os to ^{183}Re ($I^{\pi} = 5/2^+$, $T_{1/2} = 71$ d) to investigate the hyperfine interaction of ReCo(hcp). The

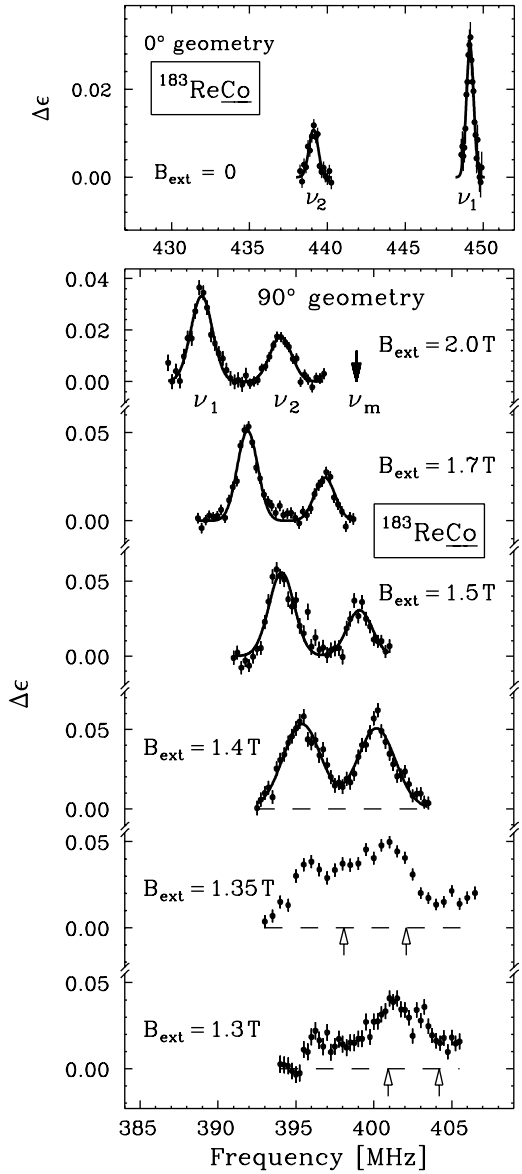

Fig. 9. ^{183}ReCo(hcp): NMR-ON spectra in the 0° and 90° geometries. The open arrows at $B_{\mathrm{ext}} = 1.35$ T and 1.3 T mark the expected positions of the ν_1 and ν_2 resonances.

ν_1 and ν_2 resonances were measured in the 0° geometry at zero field and in the 90° geometry at six different fields between 1.3 and 2 T. Figure 9 shows the resonance spectra.

Table 2. Relaxation constants in Co(hcp).

Isotope	$R^{\parallel}$ [(sK)$^{-1}$]	$R^{\perp}$ [(sK)$^{-1}$]
^{198}Au	1.02(5)[a]	0.74(5)[a]
^{191}Pt	0.43(5)[b]	0.72(5)[b]
^{188}Ir	0.93(26)	
^{183}Os	1.73(24)	
^{183}Re	5.2(9)	

[a] Ref. [27].
[b] Unpublished.

In the 90° geometry completely irregular resonance structures were observed at 1.35 T and 1.3 T. Moreover, at 1.4 T the amplitude ratio I_1/I_2 of the ν_1 and ν_2 resonances already conspicuously deviated from the expected value of about 2. The origin of those distortions of the resonance structure remains unclear: A distinct increase in the linewidth between 1.5 T and 1.3 T was found in many of our NMR-ON experiments on Co(hcp). Figure 5 illustrates this trend for ^{191}PtCo(hcp). It can be attributed to the extreme sensitivity of the magnetization behaviour in this field region to α and other parameters, which are not completely uniform over the sample. However, the spectra had never become as irregular as observed in this experiment.

Using in the 90° geometry only the data for $B_{\rm ext} \geq 1.5$ T, the *least squares* fit yielded $\alpha > 89.5°$ and

$$\nu_m^{\parallel} = 429.07(5) \text{ MHz},$$
$$\nu_m^{\perp} = 417.45(35) \text{ MHz},$$
$$\Delta\nu_Q^{\parallel} = -10.05(4) \text{ MHz},$$
$$\Delta\nu_Q^{\perp} = +4.92(7) \text{ MHz}.$$

The relative linewidth of the resonance in the 0° geometry, $\Gamma/\nu_m = 1.2(1)\times10^{-3}$, can be compared with $\Gamma/\nu_m = 3.1(6)\times10^{-3}$ for ^{183}Os at the same lattice sites. This reveals a strong element dependence of the inhomogeneous broadening of the hyperfine field.

4.6 Nuclear spin-lattice relaxation

In the course of the ^{183}OsCo(hcp) and ^{183}ReCo(hcp) experiments and an unpublished ^{188}IrCo(hcp) experiment, the nuclear spin-lattice relaxations in the 0° geometry were also measured. The relaxation of ^{188}Ir was measured at 1.0 T to avoid any cross relaxation to the ^{59}Co resonance [40], which is at zero field very close to the ν_2 resonance of ^{188}Ir. The other measurements were performed at zero field. To ensure a sufficient rf power level per frequency unit, only the ν_1 resonance was excited for ^{188}Ir and ^{183}Re, and only the ν_2 resonance for ^{183}Os.

Figure 10 shows the relaxation curves. The deduced relaxation constants are listed in Table 2. Dedicated experiments on the nuclear spin-lattice relaxation were performed for ^{198}AuCo(hcp) and ^{191}PtCo(hcp). In particular, the magnetic field dependence of the relaxation was studied. The details will be published elsewhere. Here we give only the high-field limits of the relaxation constants, which are also listed in Table 2.

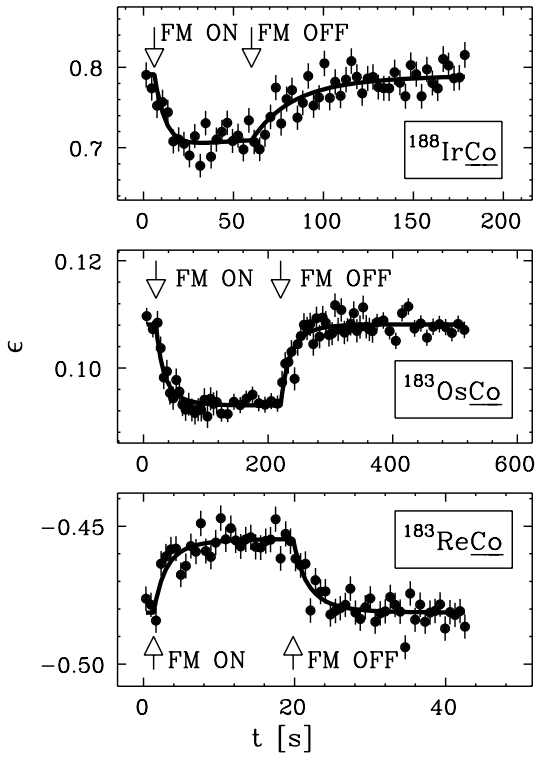

Fig. 10. NMR-ON relaxation curves of ^{188}Ir, ^{183}Os, and ^{183}Re in the 0° geometry. $T = 17.5(5)$ mK (top), 14.4(3) mK (middle), and 27(1) mK (bottom).

5 Discussion

Table 3 compiles the available data on the hyperfine interaction of the 5*d* impurities in Co(hcp). Apart from the already quoted $g(^{191}\text{Pt})$, use was made of the following nuclear moments: $g(^{197m}\text{Hg}) = 0.158$ [22], $g(^{188}\text{Ir}) = 0.306(3)$, $g(^{183}\text{Os}) = 0.180(4)$ [11], $g(^{183}\text{Re}) = 1.267(6)$ [44], $Q(^{197m}\text{Hg}) = +1.24(14)$ b [22], $Q(^{191}\text{Pt}) = -0.87(4)$ b [35], $Q(^{183}\text{Os}) = +3.12(27)$ b [45], and $Q(^{183}\text{Re}) = +2.1(2)$ b [45]. $g(^{188}\text{Ir})$ was derived from $d\nu/dB_{\rm ext} = -2.30(1)$ MHz/T for ^{188}IrCo(hcp), assuming $K = 0.00(1)$. This is at present at least as reliable as the derivation via hyperfine splitting frequencies and estimates of the hyperfine anomaly.

The EFG of HgCo(hcp) turned out to be by about a factor of 2 smaller than reported in reference [46]. The origin of this discrepancy is not clear.

5.1 Isotropic part of the hyperfine field

Figure 11 shows the hyperfine fields of the 5*d* impurities in Co(hcp) together with the hyperfine fields in Fe, Co(fcc),

Table 3. Hyperfine interaction of the 5*d* impurities in Co(hcp). $B_{\mathrm{HF}}^{\mathrm{fcc}}$ is the hyperfine field in Co(fcc).

Impurity	$B_{\mathrm{HF}}^{\mathrm{iso}}$ (T)	$B_{\mathrm{HF}}^{\mathrm{ani}}$ (T)	V_{zz}^{lat} (10^{16} V/cm^2)	$V_{z'z'}^{\mathrm{so}}$ (10^{16} V/cm^2)	$R^{\parallel}/g^2$ [(sK)$^{-1}$]	$R^{\perp}/g^2$ [(sK)$^{-1}$]	$B_{\mathrm{HF}}^{\mathrm{iso}} - B_{\mathrm{HF}}^{\mathrm{fcc}}$ (T)
Hg	−64.02(19)	−1.45(31)	−8.5(10)	−0.10(7)			
Au	−85.65(6)[a]	−1.387(11)[a]	−9.8(3)[a]	−0.016(18)[a]	11.6(6)	8.4(6)	−14.1(4)[b]
Pt	−93.0(14)	−0.818(16)	−12.9(6)	+0.035(12)	4.0(5)	6.7(5)	−12.06(18)[c]
Ir	−102.1(10)	+0.013(15)	−17.9(2)[d]	−3.79(5)[d]	9.9(28)		−7.95(9)[c]
Os	−74.6(17)	−1.12(7)	−6.9(6)	+3.72(33)	53(8)		+12.0(3)[c]
Re	−43.63(21)	−0.802(25)	−13.1(12)	−0.09(7)	3.2(6)		+4.82(6)[c]
Ta	−40.7(6)[e]		(−)12.3(4)[e]				−4.39(6)[e]
Lu	−49.59(28)[f]	−1.52(11)[f]	−17.4(3)[f]	+0.28(24)[f]			

[a] Ref. [20].
[b] $\nu_m^{\mathrm{fcc}}(^{197}\mathrm{Au})$ taken from Ref. [41], corrected for $^{197}\Delta^{198}$.
[c] ν_m^{fcc} taken from Ref. [33].
[d] Ref. [17].
[e] Refs. [42] and [43], only $B_{\mathrm{HF}}^{\parallel}$ and $V_{zz}^{\parallel}$ determined.
[f] Ref. [16].

and Ni. The hyperfine fields were divided by the spin moment μ_s of the host to reveal those differences in the systematics that go beyond a linear scaling of the hyperfine field with the magnetic moment of the host.

The trend of the 5*d* hyperfine fields in Co(hcp) is rather similar to the trend in cubic Fe, Co, or Ni. Essentially the same trend has also been observed for the 4*d* impurities [1]. It has been reproduced by *ab initio* calculations and is well understood [3,49,50].

The hyperfine fields in Co also provide a more complete experimental picture of the differences in the systematics between the various hosts. It turns out that there are no clear trends in the sequences Fe, Co, Ni or bcc, hcp, fcc. A theoretical treatment of the differences in the systematics is not available: The hyperfine fields of the 5*d* impurities have been calculated only for Fe and the results deviated distinctly from the data [49].

Figure 11 demonstrates that it is not justified to neglect the differences between the hyperfine fields in Co(hcp) and Co(fcc): The fields in the two Co phases differ by the same order of magnitude as the fields in Fe, Co, and Ni after the removal of the scaling with the host moment. This shows that the influence of the lattice symmetry and the detailed form of the band structure is remarkably large and that this influence can well be studied via the comparison of the hyperfine fields in Co(hcp) and Co(fcc).

5.2 Orbital hyperfine field

Since the HFA is an effect of the Fermi-contact interaction, it gives information on the magnitude of the noncontact part of B_{HF}. F^{nc}, the fractional contribution of the noncontact field to the total hyperfine field of isotope "2", is

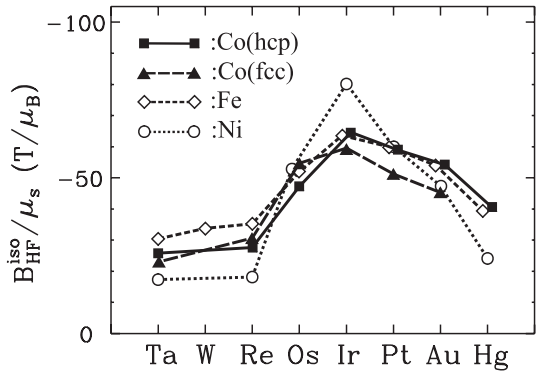

Fig. 11. Systematics of the hyperfine fields of the 5*d* impurities in Fe, Co(hcp) (isotropic part), Co(fcc), and Ni. The fields were divided by μ_s = 2.13, 1.58, and 0.56 μ_B for Fe, Co, and Ni, respectively [47,48].

given by

$$F^{\mathrm{nc}} = 1 - \frac{{}^1\Delta^2}{{}^1\Delta_c^2}, \tag{13}$$

where ${}^1\Delta_c^2$ is the HFA for a pure contact field. In this way the orbital hyperfine field, which is a direct measure of the local orbital moment, can be determined, since the noncontact part of B_{HF} is practically identical to the orbital part.

Unfortunately, the determination of F^{nc} requires the presence of a large anomaly and a reference system for which both the anomaly and F^{nc} are known. Therefore, the orbital fields have been investigated only for Au and Ir. For Au, $F_{\mathrm{Fe}}^{\mathrm{nc}} = -0.135(3)$ [51], $F_{\mathrm{Co(hcp)}}^{\mathrm{nc}} = -0.073(12)$ [20], and $F_{\mathrm{Ni}}^{\mathrm{nc}} = -0.145(21)$ [51] were determined, which corresponds to a noncontact field of $B_{\mathrm{HF}}^{\mathrm{nc}} = +6.3(10)$ T in the case of AuCo(hcp).

For Ir, at least the variation of F^{nc} with the host is now also known. From the comparison of the respective HFA's, $F_{\mathrm{Co(hcp)}}^{\mathrm{nc}} - F_{\mathrm{Fe}}^{\mathrm{nc}} = +0.012(9)$ (this work) and $F_{\mathrm{Ni}}^{\mathrm{nc}} - F_{\mathrm{Fe}}^{\mathrm{nc}} = -0.053(15)$ [52] can be derived. The comparison with the

data on Au shows that distinct differences between the systematics of the orbital and total hyperfine fields become apparent, if precise data on the HFA are available.

Using $F_{\mathrm{Fe}}^{\mathrm{nc}} = -0.11(6)$ [39], $B_{\mathrm{HF}}^{\mathrm{nc}} = +10(6)$ T would be derived for IrCo(hcp). However, this value is somewhat ambiguous, since it relies on an estimate of the orbital field of IrF_6 [39]. Moreover, the positive sign is in contradiction to circular magnetic X-ray dicroism (CMXD) measurements of the local orbital moment [53].

Precise data on the HFA's of Au and Ir in Co(fcc) would be of particular interest: The comparison with the HFA's in Co(hcp) would reveal to which extent the orbital moment is responsible for the different hyperfine fields in Co(fcc) and Co(hcp).

5.3 Anisotropic part of the hyperfine field

The anisotropy of the hyperfine field provides another possibility to study the orbital part of the hyperfine field. $B_{\mathrm{HF}}^{\mathrm{ani}}$ arises almost exclusively from the anisotropy of the orbital hyperfine field and from the spin-dipole field [5,54]. In contrast, the dominant contribution to $B_{\mathrm{HF}}^{\mathrm{iso}}$, the Fermi-contact interaction, is, as the spin moment and most features of the band structure, essentially independent of the direction of the magnetization.

The order of magnitude of the two contributions to $B_{\mathrm{HF}}^{\mathrm{ani}}$ can be estimated in the following way: According to ab initio calculations [49] and the HFA's, the orbital hyperfine field is of the order of 10 T. According to the model calculations of Appendix B, the anisotropy of the orbital moment is of the order of 10%. Thus, the orbital contribution to $B_{\mathrm{HF}}^{\mathrm{ani}}$ is expected to be of the order of 1 T.

The spin-dipole field contributes only to $B_{\mathrm{HF}}^{\mathrm{ani}}$. (At least, if the spin-orbit-induced spin-dipole field is neglected.) The respective contribution, B_{dip}, is closely related to V_{zz}^{lat}, since V_{zz}^{lat} arises from the sum of the local noncubic electron distributions of the spin-up (↑) and spin-down (↓) bands, whereas B_{dip} arises from the respective difference. (The information on V_{zz}^{lat} will thus also help to separate the orbital and spin-dipole contributions to $B_{\mathrm{HF}}^{\mathrm{ani}}$.) If only the ↑ or only the ↓ band would be relevant, the typical EFG strength, $V_{zz}^{\mathrm{lat}} = -12{\times}10^{16}$ V/cm^2, would correspond to $B_{\mathrm{dip}} = +0.8$ T or -0.8 T, respectively.

Figure 12 shows $B_{\mathrm{HF}}^{\mathrm{ani}}$ as a function of the impurity. $B_{\mathrm{HF}}^{\mathrm{ani}}$ is of the expected order of magnitude. The negative sign of $B_{\mathrm{HF}}^{\mathrm{ani}}$ for almost all 5d impurities is remarkable, since both the local spin and the local orbital moments change the sign within the 5d series [12]. In contrast, $B_{\mathrm{HF}}^{\mathrm{ani}}$ is positive for Co in Co(hcp) [6].

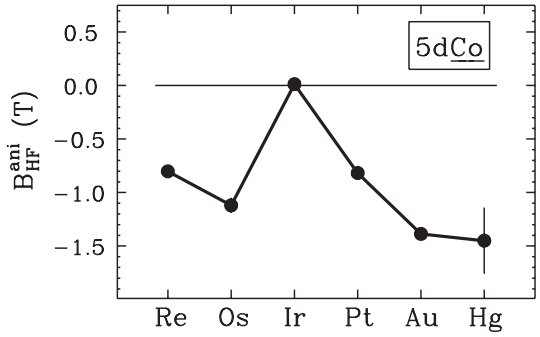

Fig. 12. Anisotropic part of the hyperfine field of the 5d impurities in Co(hcp).

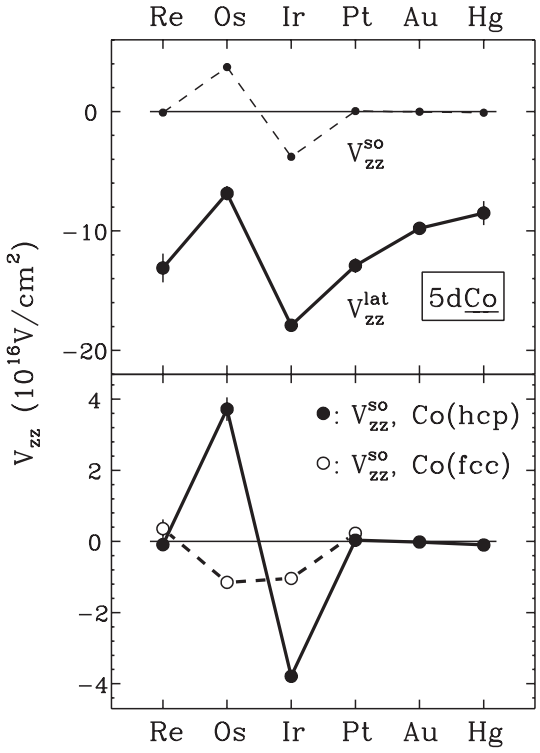

Fig. 13. EFG of the 5d impurities in Co(hcp). Top: Lattice EFG, the dashed line shows the spin-orbit EFG on the same scale. Bottom: Spin-orbit EFG, the dashed line shows the spin-orbit EFG in Co(fcc) [33].

5.4 Lattice EFG

The upper part of Figure 13 shows V_{zz}^{lat} as a function of the impurity. The EFG's of transition-metal impurities in a certain noncubic transition-metal host usually have all the same sign and the systematics is rather smooth [55,56]. Figure 13 shows that this is also true for the EFG's in Co(hcp). However, the EFG's are distinctly smaller than in other noncubic hosts, because the $c/a = 1.622$ ratio of Co(hcp) is rather close to the ideal ratio $c/a = 1.633$. The jump between Os and Ir, which is also found in $B_{\mathrm{HF}}^{\mathrm{ani}}$, might be connected to the sign change of the local spin moment, which is expected around Os.

5.5 Spin-orbit EFG

The lower part of Figure 13 shows $V_{z'z'}^{\mathrm{so}}$ as a function of the impurity. $V_{z'z'}^{\mathrm{so}}$ is a measure of the spin-orbit-induced deformation of the electron distribution. Positive $V_{z'z'}^{\mathrm{so}}$'s

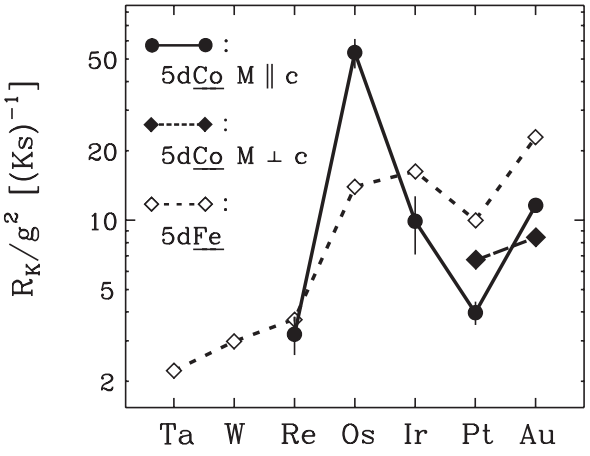

Fig. 14. Reduced nuclear spin-lattice relaxation constants in Co(hcp) and Fe. Fe data from reference [26].

correspond to oblate deformations with respect to the direction of the magnetization, negative $V^{so}_{z'z'}$'s to prolate deformations. The spin-orbit EFG's can be compared to the spin-orbit EFG's of the 5d impurities in cubic Fe, Co, and Ni, which have recently been studied in detail experimentally and theoretically [11,12]. As shown in Appendix B, there should be no fundamental difference apart from the form of the anisotropy.

Large variations of $V^{so}_{z'z'}$ from one impurity to the next, for example, are also observed in the cubic hosts. They result from the relatively large sensitivity of the effect to band structure details. That sensitivity can also be made responsible for the clearly different spin-orbit EFG's in Co(hcp) and Co(fcc), which are both shown in Figure 13. The spin-orbit EFG's of Ir and Os in Co(hcp) are of comparable magnitude as the largest EFG in the cubic hosts, $V^{so}_{z'z'}(\mathrm{IrFe}) = -4.0 \times 10^{16}$ V/cm^2 for $M \| [100]$. They are thus large, but still within the expected order of magnitude.

However, the strict division of the spin-orbit EFG's in relatively large and very small ones is unexpected and also not observed in the cubic hosts. Very small spin-orbit EFG's are expected to occur accidentally in connection with the many sign changes in the systematics, but not in such a regular manner. This implies a rather complete suppression of the spin-orbit EFG for most, but not for all impurities, which would be at variance with the present understanding of the interplay between the band structure and the spin-orbit coupling.

5.6 Nuclear spin-lattice relaxation

The spin-lattice relaxations can be compared with the spin-lattice relaxations in Fe, which have been studied experimentally and theoretically [26,57]. Figure 14 shows the systematics of the spin-lattice relaxation of the 5d impurities in Co(hcp) and Fe. The magnitude of the relaxation tends to be smaller than in Fe. It may thus also be in better agreement with the theory than in Fe, where the relaxation rates are by about a factor of 3 larger than predicted by the ab initio calculations [26].

The variation of the relaxation rate as a function of the impurity is conspicuously large and distinctly larger than in Fe. The comparison with Fe also reveals a large variation as a function of the host. Large variations in the systematics are, however, not surprising, since the nuclear spin-lattice relaxation in metals is proportional to the square of the density of states at the Fermi energy and the density of states varies rather strongly in realistic transition-metal band structures.

The anisotropy of the relaxation can be compared with band structure calculations for hexagonal transition metals, which predict anisotropies between 3% and 30% [58]. The observed differences between $R^{\|}$ and $R^{\perp}$ for AuCo(hcp) and PtCo(hcp) are thus relatively large.

For several 5d isotopes with small magnetic and large quadrupole moments, there might be an appreciable electric quadrupolar contribution to the relaxation. In this case the normalization of R to g^2 becomes inappropriate. Therefore, calculations should include the quadrupolar contribution and should directly be compared with the data of Table 2.

R_q, the electric quadrupolar contribution to R, can be estimated relative to R_o, the orbital contribution to R, by equation (26) of reference [58]. For ^{198}Au, ^{191}Pt, ^{188}Ir, ^{183}Os, and ^{183}Re one obtains $R_q/R_o \geq 0.4$, 1.2, 1.6, 3.0, and 0.1, respectively. Thus, the peak in the systematics at Os may in part be due to R_q. However, the actual importance of R_o is not known: According to the ab initio calculations, it is the dominating contribution to the magnetic relaxation [57]. But for IrFe, R_o turned out to contribute less than a third of the total magnetic relaxation [37].

6 Conclusions

Precise data on the hyperfine interaction of the 5d impurities from Re to Hg in Co(hcp) are now available. These data complete the systematics of the hyperfine interaction of these impurities in Fe, Co, and Ni. The new data are in particular of interest in the context of spin-orbit effects in magnetic transition metals: The effect of the strong spin-orbit coupling at the 5d impurities can be studied via the anisotropy of the hyperfine field, the spin-orbit EFG, and the hyperfine anomaly. The systematics of the spin-orbit EFG in Co(hcp), which is at present even qualitatively not understood, demonstrates that our understanding of the spin-orbit effects is still far from complete.

So far only the hyperfine fields of pure Co(fcc) and Co(hcp) have been investigated by ab initio calculations that also take the spin-orbit coupling into account [54]. These calculations should be extended to the 5d impurities and to the electric hyperfine interaction.

We wish to thank Prof. H.-J. Körner for the continuous support of this work and E. Smolic for experimental help.

Appendix A: Two-domain model

The two-domain model assumes an arbitrarily fine and homogeneous division of the disk-shaped sample into two sorts of domains with different orientations of the magnetization. The c axis lies within the disk plane. The domain boundaries are arranged in such a way that the divergence of the magnetization vanishes within the sample. The demagnetization field is assumed to be uniform over the sample. The magnetization behaviour can then be described by the three variables θ_1 and θ_2, which are defined in Figure 15 as the angles between the magnetization and the c axis for the two sorts of domains, and the fraction f_1 of the sample volume that is occupied by one of the two sorts. For given α and $B_{\rm ext}$, the three variables must minimize the free energy $F(\theta_1, \theta_2, f_1)$.

Since the used samples were not rotation ellipsoids, the assumed homogeneities of the demagnetization field, the magnetization, and the division of the sample into domains can only be an approximation. It has to be made to keep the number of variables manageable. This first approximation should be sufficient, if the demagnetization effects are small and the effective demagnetization factors are determined via *least squares* fit to the data.

The components of $\mathbf{B}_{\rm dem}$ parallel and perpendicular to the c axis are assumed to be given by

$$\mathbf{B}^z_{\rm dem} = -B^{(0),\parallel}_{\rm dem}(\langle\mathbf{M}\rangle^z/M),$$
$$\mathbf{B}^x_{\rm dem} = -B^{(0),\perp}_{\rm dem}(\langle\mathbf{M}\rangle^x/M).$$

Here $\langle\mathbf{M}\rangle$ is the average magnetization of the sample and $B^{(0),\parallel}_{\rm dem}$ and $B^{(0),\perp}_{\rm dem}$ are the demagnetization fields for complete magnetization of the sample parallel and perpendicular to the c axis, respectively.

If the two-domain model is applied to equation (1), one obtains the following expression for the free energy:

$$\begin{aligned} F = {} & f_1\left[K_1\sin^2\theta_1 + K_2\sin^4\theta_1\right] \\ & +(1-f_1)\left[K_1\sin^2\theta_2 + K_2\sin^4\theta_2\right] \\ & -B_{\rm ext}M\left[f_1\cos(\alpha-\theta_1) - (1-f_1)\cos(\alpha+\theta_2)\right] \\ & +(1/2)B^{(0),\parallel}_{\rm dem}M\left[f_1\cos\theta_1 - (1-f_1)\cos\theta_2\right]^2 \\ & +(1/2)B^{(0),\perp}_{\rm dem}M\left[f_1\sin\theta_1 + (1-f_1)\sin\theta_2\right]^2. \end{aligned} \quad (14)$$

The numerical minimization of this expression as a function of the three variables is rather inconvenient. Fortunately, it turns out that the solution of this minimization problem always satisfies $\theta_1 = \theta_2$. Furthermore, F can be minimized analytically with respect to f_1. The result is

$$f_1 = (1/2)\left(1 + \frac{B_{\rm ext}\cos\alpha}{B^{(0),\parallel}_{\rm dem}\cos\theta}\right) \quad (15)$$

as long as ("two-domain regime")

$$B_{\rm ext}\cos\alpha \le B^{(0),\parallel}_{\rm dem}\cos\theta, \quad (16)$$

and f_1 =1 for larger magnetic fields ("one-domain regime").

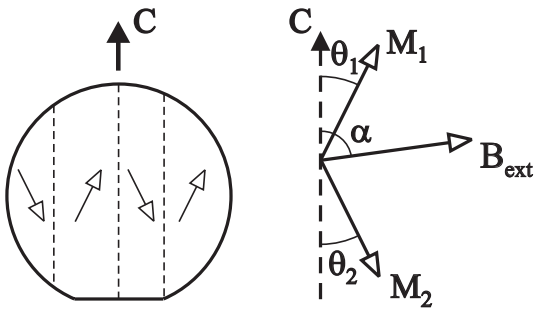

Fig. 15. Two-domain model. Left: Sketch of the division of the sample into two sorts of domains. Right: Definition of the angles α, θ_1, and θ_2.

If these results are inserted into equation (14), the problem reduces to minimize

$$\begin{aligned} F = {} & K_1\sin^2\theta + K_2\sin^4\theta - B_{\rm ext}M\sin\alpha\sin\theta \\ & +(1/2)B^{(0),\perp}_{\rm dem}M\sin^2\theta \\ & -(1/2)(B_{\rm ext}\cos\alpha)^2 M/B^{(0),\parallel}_{\rm dem} \end{aligned} \quad (17)$$

in the two-domain regime and

$$\begin{aligned} F = {} & K_1\sin^2\theta + K_2\sin^4\theta \\ & -B_{\rm ext}M(\sin\alpha\sin\theta + \cos\alpha\cos\theta) \\ & +(1/2)(B^{(0),\perp}_{\rm dem} - B^{(0),\parallel}_{\rm dem})M\sin^2\theta \\ & +(1/2)B^{(0),\parallel}_{\rm dem}M \end{aligned} \quad (18)$$

in the one-domain regime as a function of one variable, $\theta = \theta_1 = \theta_2$.

The components of the shielded external field parallel and perpendicular to the c axis are given by

$$\begin{aligned} (\mathbf{B}_{\rm ext} + \mathbf{B}_{\rm dem})^z &= \max\left[0, (B_{\rm ext}\cos\alpha - B^{(0),\parallel}_{\rm dem}\cos\theta)\right] \\ (\mathbf{B}_{\rm ext} + \mathbf{B}_{\rm dem})^x &= B_{\rm ext}\sin\alpha - B^{(0),\perp}_{\rm dem}\sin\theta. \end{aligned} \quad (19)$$

The consequences of equations (16, 17, 18), and (19) for the magnetization behaviour can shortly be described in the following way: In both types of domains the magnetization is rotated by the same angle towards the external field. If $\alpha \neq 90°$, one domain type is favoured. It grows at the expense of the other type in such a way that the component of $\mathbf{B}_{\rm ext}$ parallel to the c axis is completely shielded by $\mathbf{B}_{\rm dem}$. In the two-domain regime the magnetization is rotated towards $\mathbf{B}_{\rm ext}$ as if only the component of $\mathbf{B}_{\rm ext}$ perpendicular to the c axis would be acting on an arbitrarily thin sample with effective anisotropy field $B_a + B^{(0),\perp}_{\rm dem}$.

At a certain field strength, which is given by equation (16), only one domain is left. In the one-domain regime the only effect of the finite sample thickness is that the effective anisotropy field is $B_a + (B^{(0),\perp}_{\rm dem} - B^{(0),\parallel}_{\rm dem})$.

The consequences of the finite sample thickness for the hyperfine splitting are that θ depends in a more complicated way on $B_{\rm ext}$ and α and that $\mathbf{B}_{\rm ext}$ is partly shielded by $\mathbf{B}_{\rm dem}$. However, there is no difference between the hyperfine splittings in the two sorts of domains.

Appendix B: Spin-orbit effects in hexagonal ferromagnets

In reference [12] the relationships between the orbital moment, the spin-orbit EFG, and the band structure were analysed for cubic ferromagnets within a tight-binding scheme. We extend here the scheme to hexagonal ferromagnets. The emphasis is on the peculiarities connected with the hexagonal lattice symmetry.

Using the notation of reference [12], the orbital moment can be expressed as a function of the $\rho_i^s(e)$'s, the partial densities of states of the system without spin-orbit coupling, and ξ, the spin-orbit coupling strength, in the following way:

$$\langle l_{z'} \rangle = \xi \int^{e_F} \sum_{st} \sum_{ij} b^{st} c_{ij} \Omega_{ij}^{st}(e)\, de, \tag{20}$$

$$\Omega_{ij}^{st}(e) = -(1/\pi)\mathrm{Im}\left[G_i^s(e) G_j^t(e)\right], \tag{21}$$

$$G_i^s(e) = \mathcal{P}\left[\int \frac{\rho_i^s(e')}{(e-e')}\, de'\right] - i\pi\rho_i^s(e). \tag{22}$$

The spin-orbit-induced noncubic charge distribution, which is directly proportional to the spin-orbit EFG, can be expressed by

$$\langle l_{z'}^2 - \tfrac{l(l+1)}{3} \rangle = \xi^2 \int^{e_F} \sum_{stu} \sum_{ijk} b^{stu} c_{ijk} \Omega_{ijk}^{stu}(e)\, de + \xi^2 \int^{e_F} \sum_{stu} \sum_{ijk} \tilde{b}^{stu} \tilde{c}_{ijk} \Omega_{ijk}^{stu}(e)\, de, \tag{23}$$

$$\Omega_{ijk}^{stu}(e) = -(1/\pi)\mathrm{Im}\left[G_i^s(e) G_j^t(e) G_k^u(e)\right]. \tag{24}$$

Here, z' denotes the components along the direction of the magnetization, the superscripts s, t, and u denote the spin direction of the orbitals, the subscripts i, j, and k denote the symmetry of the orbitals, and e_F is the Fermi energy.

According to the hexagonal lattice symmetry, the following six, in general different partial densities of states have to be considered: $\rho_{E_2}^{\uparrow}$, $\rho_{E_1}^{\uparrow}$, $\rho_{A_1}^{\uparrow}$, $\rho_{E_2}^{\downarrow}$, $\rho_{E_1}^{\downarrow}$, and $\rho_{A_1}^{\downarrow}$. E_2 denotes the x^2-y^2 and xy orbitals, E_1 the xz and yz orbitals, and A_1 the $3z^2-1$ orbital. z is the direction of the c axis. The $G_i^s(e)$'s are the respective diagonal matrix elements of the unperturbed Green's function. Their real and imaginary parts are related to the partial densities of states by equation (22).

b, $\tilde{b}$, c, and $\tilde{c}$ are coefficients that describe to which extent which orbitals contribute to the respective spin-orbit effect. The nonvanishing b and c coefficients for the orbital moment are

$$b^{\uparrow\uparrow} = 1, \quad b^{\downarrow\downarrow} = -1, \tag{25}$$

$$c_{E_2E_2} = 4\cos^2\theta, \quad c_{E_1E_1} = \cos^2\theta, \quad c_{E_2E_1} = 2\sin^2\theta, \quad c_{E_1A_1} = 3\sin^2\theta. \tag{26}$$

The b, c, $\tilde{b}$, and $\tilde{c}$ coefficients for the spin-orbit-induced noncubic charge distribution are

$$b^{\uparrow\uparrow\uparrow} = 1, \quad b^{\uparrow\downarrow\uparrow} = -1, \quad b^{\downarrow\uparrow\downarrow} = -1, \quad b^{\downarrow\downarrow\downarrow} = 1, \tag{27}$$

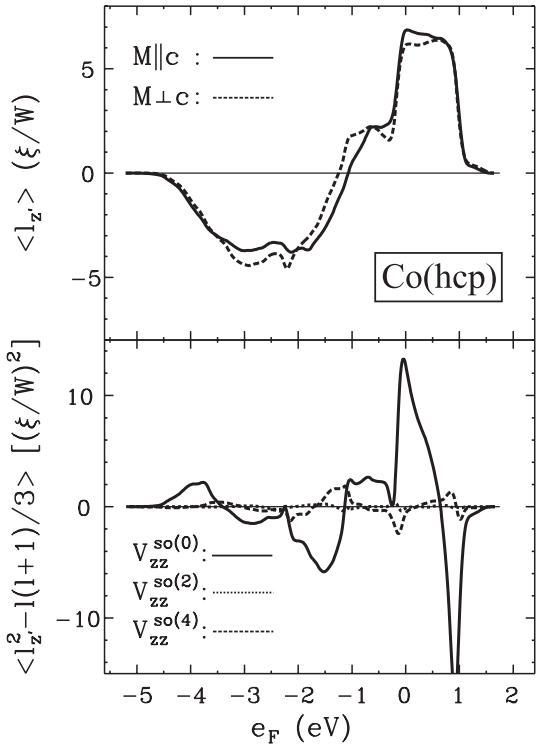

Fig. 16. Orbital moment (top) and spin-orbit-induced noncubic charge distribution (bottom) of Co(hcp) as a function of the Fermi energy. Expressed in units of ξ/W, where W = 4.7 eV is the bandwidth.

$$\begin{aligned}
c_{E_2E_2E_2} &= (4/21) + (2/21)P_2 + (48/35)P_4,\\
c_{E_2E_2E_1} &= (8/7) + (4/7)P_2 - (48/35)P_4,\\
c_{E_2E_1E_2} &= -(1/21) - (11/21)P_2 - (12/35)P_4,\\
c_{E_2E_1E_1} &= (4/7) + (2/7)P_2 - (24/35)P_4,\\
c_{E_1E_2E_1} &= (1/42) + (11/42)P_2 + (6/35)P_4,\\
c_{E_2E_1A_1} &= (5/7) - (8/7)P_2 + (12/35)P_4,\\
c_{E_1E_1E_1} &= -(1/42) - (1/84)P_2 - (6/35)P_4,\\
c_{E_1E_1A_1} &= (2/7) + (1/7)P_2 - (12/35)P_4,\\
c_{E_1A_1E_1} &= (4/7) - (13/28)P_2 + (18/35)P_4,\\
c_{A_1E_1A_1} &= (1/14) + (11/14)P_2 + (18/35)P_4,
\end{aligned} \tag{28}$$

$$\begin{aligned}
\tilde{b}^{\uparrow\uparrow\uparrow} &= 1, \quad \tilde{b}^{\uparrow\downarrow\uparrow} = 1,\\
\tilde{b}^{\downarrow\uparrow\downarrow} &= 1, \quad \tilde{b}^{\downarrow\downarrow\downarrow} = 1,
\end{aligned} \tag{29}$$

$$\begin{aligned}
\tilde{c}_{E_2E_2E_2} &= +2P_2, \quad \tilde{c}_{E_2E_1E_2} = +1P_2,\\
\tilde{c}_{E_1E_2E_1} &= -1/2P_2, \quad \tilde{c}_{E_1E_1E_1} = -1/4P_2,\\
\tilde{c}_{E_1A_1E_1} &= -3/4P_2, \quad \tilde{c}_{A_1E_1A_1} = -3/2P_2.
\end{aligned} \tag{30}$$

Here, P_2 and P_4 are abbreviations for $P_2(\cos\theta)$ and $P_4(\cos\theta)$, respectively.

To go beyond this formal analysis, equation (20) and the first term on the right hand side of equation (23) were evaluated for the partial densities of states of Co(hcp) from reference [59]. Figure 16 shows the calculated orbital moments for $\theta = 0°$ and $\theta = 90°$ as well as $V_{z'z'}^{\mathrm{so}(0)}$, $V_{z'z'}^{\mathrm{so}(2)}$,

and $V_{z'z'}^{\mathrm{so}(4)}$ as a function of the Fermi energy. The band structure of Co(hcp) serves here as a realistic example for the partial densities of states of a hexagonal system with c/a close to 1.633. The variation with e_F serves to illustrate the typical range of values that can be expected.

From equations (20–30) and the model calculation the following conclusions can be drawn: (i) Equation (20) and the first term of equation (23) are almost identical to the equations for the orbital moment and the spin-orbit EFG in cubic ferromagnets. Only the c coefficients differ, since the E_2, E_1, and A_1 orbitals have to be distinguished instead of the e_g and t_{2g} orbitals. Therefore, apart from the anisotropy, there should be no fundamental difference between the orbital moments and spin-orbit EFG's in cubic and hexagonal ferromagnets.

(ii) The second term of equation (23), which is described by the $\tilde{b}$ and $\tilde{c}$ coefficients, can be interpreted as a spin-orbit contribution to the lattice EFG, because it arises from the noncubic lattice symmetry and not from the magnetism of the system: It is absent in cubic ferromagnets and vanishes for a spherical electron distribution ($\rho_{E_2} = \rho_{E_1} = \rho_{A_1}$). It shows a P_2 dependence as the $z'z'$ component of the lattice EFG. It is not restricted to magnetic systems, since the contributions from the different spin directions are summed up in the form $\uparrow\uparrow\uparrow + \uparrow\downarrow\uparrow + \downarrow\uparrow\downarrow + \downarrow\downarrow\downarrow$. The term should be of the same order of magnitude as the spin-orbit EFG, but should be only a minor contribution to the lattice EFG.

(iii) The orbital moment is anisotropic already in first-order perturbation theory, whereas it is isotropic in the cubic lattice symmetry. The anisotropy is typically of the order of 10% and can be described by a $P_2(\cos\theta)$ term.

(iv) As in the cubic lattice symmetry, the spin-orbit EFG is anisotropic already in the lowest-nonvanishing-order perturbation theory. The anisotropy can be described by a $P_2(\cos\theta)$ and a $P_4(\cos\theta)$ term. In principle, $V_{z'z'}^{\mathrm{so}(2)}/V_{z'z'}^{\mathrm{so}(0)}$ and $V_{z'z'}^{\mathrm{so}(4)}/V_{z'z'}^{\mathrm{so}(0)}$ can adopt any value. Typically, however, they are of the order of 10%. The anisotropy of the spin-orbit EFG is thus distinctly smaller than in the cubic lattice symmetry.

References

1. G.N. Rao, Hyperfine Interact. **24/26**, 1119 (1985)
2. J. Kanamori, H.K. Yoshida, K. Terakura, Hyperfine Interact. **9**, 363 (1981)
3. H. Akai, M. Akai, S. Blügel, B. Drittler, H. Ebert, K. Terakura, R. Zeller, P.H. Dederichs, Prog. Theor. Phys. Suppl. **101**, 11 (1990)
4. S. Cottenier, H. Haas, Phys. Rev. B **62**, 461 (2000)
5. G.J. Perlow, C.E. Johnson, W. Marshall, Phys. Rev. **140**, A875 (1965)
6. M. Kawakami, T. Hihara, Y. Koi, T. Wakiyama, J. Phys. Soc. Jpn **33**, 1591 (1972)
7. P. Bruno, Phys. Rev. B **39**, 865 (1989); in *Ferienkurse des Forschungszentrum Jülich*, edited by R. Hölze (Forschungszentrum Jülich, 1993), Chap. 24
8. O. Hjortstam, K. Baberschke, J.M. Wills, B. Johansson, O. Eriksson, Phys. Rev. B **55**, 15026 (1997)
9. O. Erikson, B. Johansson, R.C. Albers, A.M. Boring, M.S.S. Brooks, Phys. Rev. B **42**, 2707 (1990)
10. T. Huhne, C. Zecha, H. Ebert, P.H. Dederichs, R. Zeller, Phys. Rev. B **58**, 10236 (1998)
11. G. Seewald, E. Zech, E. Hagn, R. Kleyna, M. Voß, A. Burchard, ISOLDE Collaboration, Phys. Rev. B **66**, 174401 (2002)
12. G. Seewald, E. Zech, H. Haas, Phys. Rev. B **66**, 174402 (2002)
13. H. Enokiya, J. Phys. Soc. Jpn **42**, 796 (1977)
14. D. Fekete, H. Boasson, A. Grayevski, V. Zevin, N. Kaplan, Phys. Rev. B **17**, 347 (1978)
15. G. Seewald, E. Hagn, E. Zech, K. Freitag, P. Herzog, Phys. Rev. B **59**, 13948 (1999)
16. C. König, B. Hinfurtner, E. Hagn, E. Zech, R. Eder, Phys. Rev. C **54**, 1027 (1996)
17. G. Seewald, B. Hinfurtner, E. Hagn, E. Zech, D. Forkel-Wirth, R. Eder, ISOLDE Collaboration, Phys. Rev. Lett. **80**, 3638 (1998)
18. G. Seewald, E. Hagn, B. Hinfurtner, E. Zech, D. Forkel-Wirth, R. Eder, and ISOLDE Collaboration, Phys. Rev. Lett. **77**, 5016 (1996)
19. B. Hinfurtner, E. Hagn, E. Zech, R. Eder, and ISOLDE Collaboration, Phys. Rev. Lett. **64**, 2188 (1990)
20. R. Schmid, B. Hinfurtner, E. Hagn, E. Zech, M. Deicher, Phys. Lett. A **174**, 155 (1993)
21. F. Ono, J. Phys. Soc. Jpn **50**, 2564 (1981)
22. P. Raghavan, At. Data Nucl. Data Tables **42**, 189 (1989)
23. M. Kontani, T. Hioki, Y. Masuda, J. Phys. Soc. Jpn **32**, 416 (1972)
24. M. Kopp, E. Klein, Hyperfine Interact. **11**, 153 (1981)
25. H.D. Rüter, W. Haaks, E.W. Duczynski, E. Gerdau, D. Visser, L. Niesen, Hyperfine Interact. **9**, 385 (1981)
26. T. Funk, E. Beck, W.D. Brewer, C. Bobek, E. Klein, J. Magn. Magn. Mater. **195**, 406 (1999)
27. O. Schramm, diploma thesis, TU München, 1992
28. G. Seewald, E. Hagn, E. Zech, M. Deicher, unpublished
29. E. Matthias, R.J. Holliday, Phys. Rev. Lett. **17**, 897 (1966)
30. P.T. Callaghan, P.J. Back, D.H. Chaplin, Phys. Rev. B **37**, 4900 (1988)
31. P.J. Back, D.H. Chaplin, P.T. Callaghan, Phys. Rev. B **37**, 4911 (1988)
32. G. Seewald, E. Hagn, E. Zech, D. Forkel-Wirth, Nucl. Phys. A **602**, 41 (1996)
33. G. Seewald, E. Hagn, E. Zech, Phys. Rev. B **63**, 054428 (2001)
34. F. Bacon, J.A. Barclay, W.D. Brewer, D.A. Shirley, J.E. Templeton, Phys. Rev. B **5**, 2397 (1972); E. Klein in *Low-Temperature Nuclear Orientation*, edited by N.J. Stone, H. Postma (North Holland, Amsterdam, 1986), Chap. 12
35. Th. Hilberath, St. Becker, G. Bollen, H.-J. Kluge, U. Krönert, G. Passler, J. Rikovska, R. Wyss, ISOLDE Collaboration, Z. Phys. A **342**, 1 (1992)
36. G. Seewald, E. Hagn, E. Zech, D. Forkel-Wirth, A. Burchard, ISOLDE Collaboration, Phys. Rev. Lett. **78**, 1795 (1997)
37. G. Seewald, E. Zech, H.-J. Körner, D. Borgmann, M. Dietrich, ISOLDE Collaboration, Phys. Rev. Lett. **88**, 057601 (2002)
38. P.A. Moskowitz, Phys. Lett. B **118**, 29 (1982)
39. F.E. Wagner, Hyperfine Interact. **13**, 149 (1983)
40. G. Seewald, E. Hagn, E. Zech, Phys. Rev. Lett. **78**, 5002 (1997)

41. M. Kawakami, H. Enokiya, T. Okamoto, J. Phys. F: Met. Phys. **15**, 1613 (1985)
42. S.C. Bedi, M. Forker, Phys. Rev. B **47**, 14948 (1993)
43. J.G. Marques, A.A. Melo, J. C. Soares, E. Alves, M. F. da Silva, K. Freitag, *Proceedings of the 10th International Conference on Hyperfine Interactions*, edited by M. Rots, A. Vantomme, J. Dekoster, R. Coussement, G. Langouche [Hyperfine Interact. (C), 1996], p. 33
44. S. Ohya, K. Nishimura, N. Mutsuro, Hyperfine Interact. **36**, 219 (1987)
45. E. Hagn, Hyperfine Interact. **22**, 19 (1985)
46. J.G. Marques, J.G. Correia, A.A. Melo, J.C. Soares, E. Alves, M.F. da Silva, J. Appl. Phys. **76**, 6906 (1994)
47. R. Pauthenet, J. Appl. Phys. **53**, 8187 (1982)
48. D. Bonnenberg, K.A. Hempel, H.P. Wijn, in *Magnetic Properties of Metals*, edited by H.P. Wijn, Landolt-Börnstein, Group III, Vol. 19a (Springer, Berlin, 1986)
49. H. Ebert, R. Zeller, B. Drittler, P.H. Dederichs, J. Appl. Phys. **67**, 4576 (1990)
50. V.S. Stepanyuk, R. Zeller, P.H. Dederichs, I. Mertig, Phys. Rev. B **49**, 5157 (1994)
51. P.C. Riedi, E. Hagn, Phys. Rev. B **30**, 5680 (1984)
52. E. Hagn, K. Leuthold, E. Zech, H. Ernst, Z. Phys. A **295**, 385 (1980)
53. V.V. Krishnamurthy, M. Suzuki, N. Kawamura, T. Ishikawa, Y. Kohori, Hyperfine Interact. **136/137**, 361 (2002)
54. G.Y. Guo, H. Ebert, Phys. Rev. B **53**, 2492 (1996)
55. R. Vianden, Hyperfine Interact. **35**, 1079 (1987)
56. E. Hagn, M. Zahn, E. Zech, Phys. Rev. B **28**, 3130 (1983)
57. H. Akai, Hyperfine Interact. **43**, 255 (1988)
58. T. Asada, K. Terakura, J. Phys. F: Met. Phys. **12**, 1387 (1982)
59. S. Ishida, J. Phys. Soc. Jpn **33**, 369 (1972)